Contrast cancellation technique applied to digital x-ray imaging using silicon strip detectors

C. Avila, J. Lopez, and J. C. Sanabria
Departamento de Fisica, Universidad de Los Andes, Bogota, Colombia

G. Baldazzi, D. Bollini, and M. Gombia
Dipartimento di Fisica dell'Università di Bologna and INFN, Bologna, Italy

A. E. Cabal, C. Ceballos, and A. Diaz Garcia
CEADEN, Havana, Cuba

M. Gambaccini, A. Taibi, A. Sarnelli, and A. Tuffanelli
Dipartimento di Fisica dell'Università di Ferrara and INFN, Ferrara, Italy

P. Giubellino, A. Marzari-Chiesa, F. Prino,[a] and E. Tomassi
Dipartimento di Fisica Sperimentale dell'Università di Torino and INFN, Torino, Italy

P. Grybos, M. Idzik, K. Swientek, and P. Wiacek
Faculty of Physics and Applied Computer Science, AGH University of Science and Technology, Cracow, Poland

L. M. Montaño
CINVESTAV, Mexico City, Mexico

L. Ramello and M. Sitta
Dipartimento di Scienze e Tecnologie Avanzate dell'Università del Piemonte Orientale and INFN, Alessandria, Italy

(Received 8 April 2005; revised 7 September 2005; accepted for publication 24 September 2005; published 22 November 2005)

Dual-energy mammographic imaging experimental tests have been performed using a compact dichromatic imaging system based on a conventional x-ray tube, a mosaic crystal, and a 384-strip silicon detector equipped with full-custom electronics with single photon counting capability. For simulating mammal tissue, a three-component phantom, made of Plexiglass, polyethylene, and water, has been used. Images have been collected with three different pairs of x-ray energies: 16–32 keV, 18–36 keV, and 20–40 keV. A Monte Carlo simulation of the experiment has also been carried out using the MCNP-4C transport code. The Alvarez-Macovski algorithm has been applied both to experimental and simulated data to remove the contrast between two of the phantom materials so as to enhance the visibility of the third one. © *2005 American Association of Physicists in Medicine*. [DOI: 10.1118/1.2126568]

Key words: dual-energy x-ray imaging, mammography, silicon microstrip detectors, MCNP simulations

I. INTRODUCTION

Breast cancer is a common tumoral affliction among the female population.[1,2] As for other cancer types, early detection greatly improves the prognosis and the patient survival probability. Traditionally, conventional screen-film radiography is used for initial detection and subsequent follow-up of suspicious cancerous lesions within the breast. An important aspect of mammography is its use in screening programs, where many healthy patients are submitted to a radiation dose, which must be therefore kept as low as possible. For this reason, digital mammography systems based on particle detectors[3–7] (such as phosphor or scintillator coupled to charge coupled device (CCD) or thin film transistor) are gradually replacing the traditional systems based on screen +film. The use of digital systems has also the advantage of postprocessing image capability which allows to increase the possibility of detecting small lesions.

The main limitation in the quality of mammographic images is that the signal arising from pathologic tissues in the energy range between 17 and 20 keV is superimposed on the high contrast resulting from the nonuniform structure of healthy (glandular and fat) tissues in the breast and this may prevent the detection of small lesions, especially in the presence of dense glandular tissue. Cancers may be missed when calcifications are obscured by the contrast between soft tissues in the breast which gives rise to a "cluttered" background.

Dual-energy radiography is an effective technique proposed by Alvarez and Macovski[8] and Lehmann *et al.*[9], which allows removal of contrast between pairs of materials by a combination of two images acquired at different energies (low and high energies). In this way it is possible to improve the contrast of details of interest by suppressing the cluttered background.[10]

Dual-energy radiography has not fully evolved into a routine clinical examination yet, mainly because of the limitations of conventional imaging systems. Dual-energy studies have been performed in the past both with dual-kVp approach[11] (in which the x-ray tube potential is switched between two voltages) and with single-exposure imaging using two x-ray detectors with different energy sensitivities.[12] Both these methods require high kVp settings (the optimum energies are evaluated in Ref. 10 as 19 and 68 keV). The main limitation of dual kVp imaging comes from the double exposure required to obtain the images which implies motion artifacts and high doses delivered to the patient. The single-exposure imaging is limited by higher tube loading factors and higher doses than the standard practice.

These drawbacks may be overcome by using (quasi-) monochromatic x-ray beams, where the removal of the energy components with low content of diagnostic information from the spectrum, leads to a reduction of the dose administered to patients while maintaining (or improving) the image quality. A dual-energy beam made of two (quasi-) monochromatic beams of different energies superimposed in space also solves the problem of double exposure and allows single-shot imaging. Truly monochromatic synchrotron radiation would be the ideal source for the dual-energy technique, but synchrotrons are available only in a few locations and at high cost, so this solution is not proposable for clinical practice.

A compact source, which allows to generate quasi-monochromatic beams with a conventional x-ray tube, has recently become available,[13] offering an interesting image quality at a much reduced cost. A silicon strip detector and the associated very large scale integrated electronics with single-photon counting capability[14–18] have been developed in recent years for detection of x rays from this quasi-monochromatic source. The detector is exposed directly to the x-ray beam; no photon converter is used so as to avoid spatial resolution limitations. The single-photon counting design has been chosen because it provides almost infinite dynamic range and does not add noise to the acquired signal, thus allowing to obtain the highest possible signal-to-noise ratio (SNR).[4]

Such an imaging system (laminar beam+unidimensional detector) requires scanning to reconstruct a two-dimensional (2D) image and therefore, due to the longer time required for the examination, it may not be adequate for mammographies in screening programs. However, thanks to the enhanced contrast, it is a good candidate for clinical practice as a second examination in the cases in which the conventional examination leads to an uncertain diagnosis (e.g., in the case of dense breasts where masses and microcalcifications are hardly visualized by the conventional examination).

The aim of the present work is to investigate the imaging capabilities of the system described above, using a tissue-equivalent phantom made of three components. We consider whether it could be possible to apply dual-energy radiography to the breast, hypothetically principally composed of three (glandular, adipose, and cancerous) tissues, in order to remove the clutter due to the distribution of healthy tissues and, as a consequence, enhance the intrinsic contrast of the pathology. Mammographic imaging experiments were performed in 2002 and 2003 at the quasi-monochromatic beam facility located at University of Ferrara; preliminary results were previously reported.[19,20] The dual-energy analysis procedure was applied to the data obtained from the experiment as well as to those obtained from a Monte Carlo simulation of the experimental setup. For the simulation the particle transport code MCNP-4C was used.[21]

Previous results using the contrast cancellation algorithm for dual-energy mammographic imaging both with synchrotron radiation[22] and the quasi-monochromatic x-ray source[23] have been already obtained and published by some of the authors of this work. For these images the same three-component phantom and different detectors (namely a Fuji BAS-MP 2025 storage phosphor image plate and a EEV 05-20 CCD) have been used.

II. CONTRAST CANCELLATION ALGORITHM

The contrast cancellation algorithm proposed in Refs. 8 and 9 is based on the decomposition of the mass attenuation coefficient of any material ξ in a linear combination of the coefficients of two basis materials α and β

$$\frac{\mu_\xi(E)}{\rho_\xi} = a_1 \frac{\mu_\alpha(E)}{\rho_\alpha} + a_2 \frac{\mu_\beta(E)}{\rho_\beta}. \tag{1}$$

Multiplying Eq. (1) by the thickness t_ξ and density μ_ξ of the material ξ, the logarithmic transmission can be expressed as a combination of the linear attenuation coefficients of the base materials α and β

$$M = \mu_\xi t_\xi = A_1 \mu_\alpha(E) + A_2 \mu_\beta(E). \tag{2}$$

For any material ξ, A_1 and A_2 represent the thickness of basis materials α and β that would provide the same x-ray transmission as material ξ.

If the logarithmic transmission M of an absorbing material is measured at two different energies (low and high), the following system of equations is obtained:[9,22]

$$\begin{cases} M_l = A_1 \mu_\alpha(E_\ell) + A_2 \mu_\beta(E_\ell) \\ M_h = A_1 \mu_\alpha(E_h) + A_2 \mu_\beta(E_h). \end{cases} \tag{3}$$

The solution of the system provides the coefficients A_1 and A_2

$$\begin{aligned} A_1 &= \frac{M_h \mu_\beta(E_\ell) - M_\ell \mu_\beta(E_h)}{\mu_\alpha(E_h)\mu_\beta(E_\ell) - \mu_\beta(E_h)\mu_\alpha(E_\ell)} \\ A_2 &= \frac{M_\ell \mu_\alpha(E_h) - M_h \mu_\alpha(E_\ell)}{\mu_\alpha(E_h)\mu_\beta(E_\ell) - \mu_\beta(E_h)\mu_\alpha(E_\ell)}. \end{aligned} \tag{4}$$

Aluminum and Lucite (methylmethacrylate polymer) have been used in the past as basis materials. For mammography, however, a choice of basis materials with closer attenuation coefficients is required, because of the small differences between the coefficients of normal and tumoral breast tissues. Polymethylmethacrylate (PMMA) and polyethylene (PE) have been chosen as basis materials (α and β).[22]

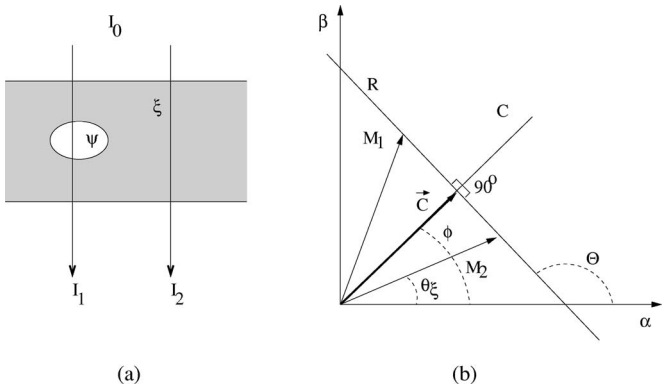

FIG. 1. (a) Transmission of a monochromatic x-ray beam I_0 through a cavity composed of two different materials (ξ and ψ). I_1 and I_2 are the intensities transmitted from the incident beam with respect to two different points in the cavity. (b) Logarithmic transmissions represented in a vector form (M_1 and M_2) on a plane formed by the basis materials (α and β). All vectors of logarithmic transmission through the cavity define the line R. C is the projection direction, characterized by the angle ϕ, that is the contrast cancellation angle between ξ and ψ; ϑ_ξ is the characteristic angle of the material ξ.

Lehmann *et al.*[9] have shown the convenience of representing M by a vector in a two-dimensional basis plane. The length $L=\sqrt{A_1^2+A_2^2}$ of the vector is proportional to the thickness t_ξ, while the angle $\theta_\xi=\tan^{-1}(A_1/A_2)$ is the characteristic angle of material ξ in the basis plane.

If a further material ψ replaces some volume of material ξ [see Fig. 1(a)], then the contrast be-tween ξ and ψ can be forced to vanish. In Fig. 1(a) I_1 is the fraction of the beam I_0 transmitted through a thickness of material ξ and a thickness of material ψ, while I_2 is the fraction of I_0 transmitted only through material ξ.

In Fig. 1(b) the vertices of the vectors M_1 and M_2 (associated, respectively, with I_1 and I_2) lie on a line R with slope

$$\Theta = \arctan\left[\frac{\rho_\alpha}{\rho_\beta}\left(\frac{\rho_\xi a_{2\xi}-\rho_\psi a_{2\psi}}{\rho_\xi a_{1\xi}-\rho_\psi a_{1\psi}}\right)\right] \tag{5}$$

which only depends on the characteristics of the two basis materials (α and β) and the two materials ξ and ψ. The radiographic images are obtained by associating a gray level with the modulus of each vector. If a direction C perpendicular to R is considered, the projections of logarithmic transmission vectors M_1 and M_2 along C have the same modulus so that the gray level associated with materials ξ and ψ in the projected image is the same. The direction C is defined by an angle $\phi=\Theta-90°$ in the basis plane which is called the contrast cancellation angle. Knowing the attenuation coefficients of the materials at both energies, a theoretical value of ϕ can be computed using Eq. (5).

III. EXPERIMENTAL SETUP

A schematic representation of the experimental setup is shown in Fig. 2. The polychromatic beam produced by a W anode and Be-window x-ray tube is diffracted via a mosaic crystal monochromator. The mean energy E of the quasi-monochromatic beam is given by the well-known Bragg formula

$$E=\frac{nhc}{2d\sin\vartheta_B}, \tag{6}$$

where d is the distance between the lattice planes of the highly oriented pyrolitic graphite crystal, $n=1,2,3\ldots$ is the diffraction order, h is the Planck constant, and ϑ_B the Bragg angle.[23] The crystal has a measured mosaic spread of 0.26°, a thickness of 1.0 mm and a surface area of 60.0 $\times$ 28.0 mm^2.[24]

Using the first two diffraction orders a dichromatic beam is produced. Three pairs of energies have been used for these measurements: 16–32 keV, 18–36 keV, and 20–40 keV. The beam spot is rectangular, with dimensions of 68 mm along the vertical axis and 8 mm in the horizontal direction. As a first approximation, the beam can be considered as parallel and the beam divergence (which could give rise to parallax errors) neglected. For more details about spatial resolution of the beam see Ref. 25. An energy gradient along the horizontal direction is present. To quantify this gradient, the beam energy as a function of position along this direction has been measured with a CdTe detector. The measured energy variation at nominal beam energy of 20 keV is 1.8 keV over a distance of 8 mm, corresponding to a percent energy gradient $1/E\,dE/dx=1.1\%$ mm^{-1}. Due to this energy gradient, a slight misalignment of the detector with respect to the center of the beam leads to a difference between the nominal and the real energy of the incident photons.

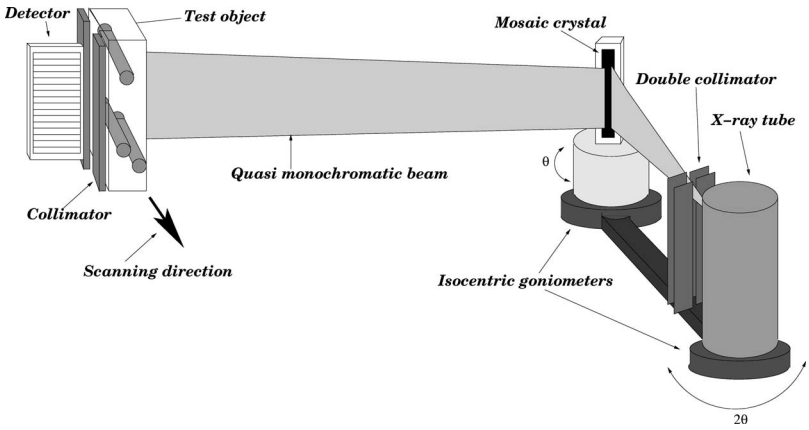

FIG. 2. Schematic representation of the experimental setup.

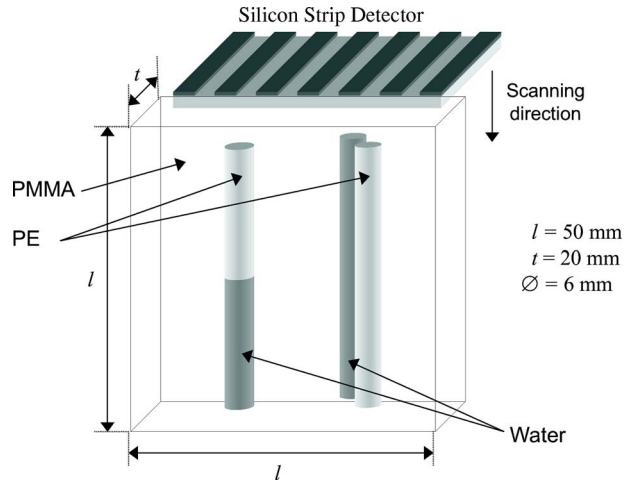

FIG. 3. Schematic representation of the mammographic phantom used for the experimental measurements.

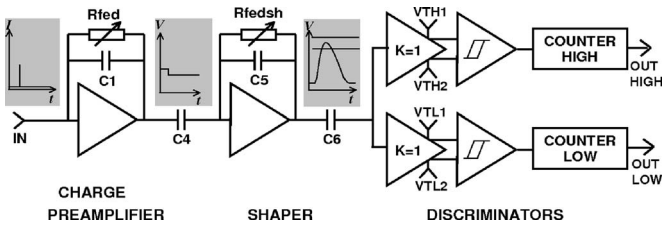

FIG. 4. Block diagram of a single electronic channel of the RX64DTH ASIC.

The three-component phantom used for the experimental measurements is sketched in Fig. 3. It is a Plexiglas (PMMA) slab of size $50\times50\times20$ mm^3 in which three cylinders of 6 mm diameter are contained. One is partially in polyethylene (PE) and partially in water, another is made of PE and is partially superimposed to the third which is filled with water. The choice of the three phantom materials (PMMA, polyethylene, and water) is due to their similar transmission properties with respect to breast tissues, as can be seen in Table I. The detection of water details on the cluttered background originating from the contrast between PMMA and PE is analogous to the task of distinguishing calcifications in a mixture of glandular and adipose tissues.

For detecting the x rays a silicon strip detector equipped with full-custom electronics with single-photon counting capability has been used. The system is intended for imaging with x rays of relatively low energy (10–40 keV) and has single-photon counting capability in order to minimize the dose required to obtain a good quality diagnostic image.

The main characteristics of the detector are summarized in Table II. Silicon has been chosen as the detector material out of simplicity and reliability considerations; however, due to the low photoelectric absorption probability in the standard thickness of 300 μm, the strips must be oriented parallel to the incoming x rays.[27] In this way, we avoid the use of a photon converter which would enhance the detecting efficiency at the expense of a limitation in the spatial resolution. A strip length of 1 cm provides acceptable conversion efficiency at the upper energy of 40 keV. Taking into account the conversion probability in the active strips and the absorption in the inactive region around the strips (765 μm thick in our case), a detection efficiency of $\approx$45% at 20 keV and of $\approx$78% at 35 keV is obtained (for more details see Fig. 4 in Ref. 17).

The strip pitch of 100 μm was chosen both because it is a standard in digital mammography and because no significant gain in spatial resolution is expected when going to lower values such as 50 μm.[14] Furthermore, a contamination in the low energy image is present because the detected spectrum of the high energy component of the beam presents a tail at lower energies due both to Compton scattering and charge sharing between strips. A detailed simulation has shown[28] that this contamination is roughly doubled when decreasing the strip pitch from 100 to 50 μm, as a consequence of the larger charge-sharing effect.

Two detector prototypes with different readout electronics for single-photon counting have been developed and tested. The readout chain of the first prototype is based on the RX64 application-specific integrated circuit (ASIC)[16] which consists of 64 analog channels and 64 independent counters to process signals and store data from 64 strips of the silicon detector. A second prototype is equipped with the RX64DTH ASIC featuring a double threshold for each analog channel.[18] This ASIC provides the possibility of counting photons for two different discriminator thresholds, thereby allowing a straightforward use of dual-energy imaging techniques. Furthermore, a new structure of CR-$(RC)^2$ shaper stage has been implemented and the discriminator structure redesigned, in order to make the circuit parameters (gain, noise, and matching performance from channel to channel) adequate for the medical imaging applications with higher x-ray energy ranges (up to 44 keV).

The block diagram of a single electronic channel of the RX64DTH ASIC is shown in Fig. 4. The channel consists of four basic blocks: charge sensitive preamplifier, shaper, two independent discriminators, and two independent 20 bit pseudo-random counters. The charge preamplifier integrates the current input signal from a silicon strip detector into a voltage signal. The shaper circuit provides noise filtering and semi-Gaussian pulse shaping. Each front-end channel is equipped with two discriminators, which work with separate thresholds: low and high. Pulses above the low threshold and pulses above the high threshold are counted independently by the two counters integrated in each readout channel. The counting rate of the single analogue channel is about 100 kHz for statistically distributed photons from the x-ray tube.

Six RX64 (RX64DTH) ASICs are needed to serve 384 out of the 400 strips of a silicon strip detector. The sensor and the integrated circuits are glued on a printed circuit board which contains the signal and power lines and also provides mechanical support. The detector and the ASICs are connected together using wire bonding and a pitch adapter printed on glass (see Fig. 5).

TABLE I. The linear attenuation coefficients of breast tissues (taken from Ref. 26) compared to the ones of the phantom materials for some interesting energies.

Energy (keV)	Breast tissue			Phantom materials		
	μ_{fat} (cm^{-1})	μ_{fibr} (cm^{-1})	μ_{carc} (cm^{-1})	μ_{PE} (cm^{-1})	μ_{PMMA} (cm^{-1})	μ_{water} (cm^{-1})
18	0.558	1.028	1.085	0.490	0.850	1.042
20	0.456	0.802	0.844	0.410	0.680	0.810
25	0.322	0.506	0.529	0.305	0.459	0.508
30	0.264	0.378	0.392	0.257	0.361	0.376
40	0.215	0.273	0.281	0.225	0.280	0.270

The calibration of the system, i.e., the measurement of gain, offsets, and equivalent noise charge (ENC) is obtained by means of discriminator threshold scans for given energies of incoming x-ray radiation, as described in Ref. 27. The x-ray energies used for such a calibration are obtained from $K\alpha$ fluorescence of photons emitted by a Cu-anode x-ray tube on six different targets (Ge, Zr, Nb, Mo, Ag, Sn). For the RX64 ASICs mounted on the 384-channel module we have measured an average gain of 64 μV/el with ENC $\approx$170 el. rms for shaper peaking time T_p=0.7 μs. The measured average gain for the RX64DTH integrated circuit is about 47 μV/el with ENC=200 el. rms for T_p=0.8 μs, i.e., 0.72 keV (rms) in terms of deposited energy in silicon. The spreads of gain and discriminator threshold inside a single 64-channel IC RX64 or RX64DTH are negligible compared to ENC, so the effective threshold spread does not limit the performance of our multichannel system in applications like, e.g., dual-energy mammography.

Data have been collected with a program written in LABVIEW 6.0 (National Instruments), while image processing has been performed with two different software tools: IGOR PRO 4.05A[29] and MATLAB.[30]

IV. IMAGE ACQUISITION AND CORRECTION

Profiles of the phantom were taken with three energy settings, namely 16–32, 18–36, and 20–40 keV, which cover the range of energies needed to ensure a good balance between the photon statistics at low and high energy for breasts of different densities and thicknesses (see Refs. 22 and 23).

The two beams are superimposed in space. The high energy image is obtained by setting the discriminator threshold in the region between the two x-ray energies, while the low energy image is obtained by setting the threshold below the lower x-ray energy and then subtracting the counts measured with the higher threshold. The discriminator thresholds for each energy pair have been chosen according to the results of threshold scan measurements performed with the detector irradiated by the dichromatic beam.

TABLE II. Detector characteristics.

Issue	Value
Strip length	10 mm
Thickness	300 μm
Dead region (edge-on configuration)	765 μm
Strip pitch	100 μm
Strip width	80 μm
Strips	384
Leakage current	$<$100 pA/strip
Total strip capacitance	$\sim$3 pF

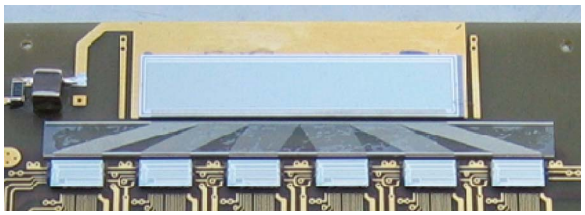

FIG. 5. The 384-strip detector together with the pitch adapter and six RX64DTH ASICs.

Two sets of images have been collected using two different detectors. In the first set of images, the detector equipped with RX64 ASIC was used and two separate exposures to the dichromatic beam with different discriminator thresholds were therefore necessary. The second set of images was collected with the detector equipped with the RX64DTH ASIC. The double threshold allows the acquisition of the low energy and high energy images within the same exposure.

The tube settings for these measurements are summarized in Table III together with exposure times for each profile and photon statistics. Two different operation modes of the tube have been used with the two different detectors: long exposure time (20 s) and low flux in the case of the RX64DTH based detector, higher flux and shorter exposure time (4 s) with the RX64 based detector. [The first operation mode has the advantage of a lower counting rate as well as a smaller tube heating. It is a good choice for imaging tests, but it is not optimal, given the very long time needed for a full scan, for clinical application].

A 2D image of the phantom should be generated by scanning the phantom in the direction perpendicular to the beam axis. The pixel size of the image is determined by the strip pitch (100 μm) along the detector and by the detector thickness (300 μm) in the scanning direction, resulting in a 0.1 $\times$0.3 mm^2 pixel. Due to the translational symmetry of the phantom, scanning along the direction indicated in Fig. 3 was replaced by two groups of 20 measurements each at two fixed positions in the two halves of the phantom. In such a way a 384$\times$40 pixel matrix was obtained, just as though a scanning of the phantom at 40 different positions along the axis of the cylinders was made. By associating a gray level to the number of counts, the raw images at low and high threshold are obtained, as demonstrated in Figs. 6(a) and 6(b), referring to the detector equipped with RX64DTH ASICs.

The statistics collected are reported in Table III. The numbers of photons are the average counts per strip in a PMMA region of the phantom and therefore correspond to the number of detected x rays after traversing 2 cm of PMMA. The number of photons per cm^2 impinging on the phantom sur-

TABLE III. Tube settings used for the data taking. The photon counts are the average counts per strip measured for an x-ray beam traversing 2 cm of PMMA. The photon flux on the phantom surface is estimated from these average counts taking into account the detector efficiency and the PMMA absorption.

E_{Beam}		HV_{tube}	I_{tube}	t_{exp}	No. detected photons		Photon flux	
Low	High				Low	High	Low	High
(keV)		(kV)	(mA)	(s)	(counts/strip)		(cm^{-2} s^{-1})	
Detector equipped with RX64								
16	32	49	55	4	8700	6900	$2.9\cdot10^{8}$	$1.4\cdot10^{7}$
18	36	49	55	4	19000	5100	$2.4\cdot10^{8}$	$1.0\cdot10^{7}$
20	40	49	55	4	32300	2600	$2.2\cdot10^{8}$	$5.1\cdot10^{6}$
Detector equipped with RX64DTH								
16	32	49	5	20	2500	2800	$1.7\cdot10^{7}$	$1.1\cdot10^{6}$
18	36	49	5	20	9500	2000	$2.4\cdot10^{7}$	$7.8\cdot10^{5}$
20	40	49	5	20	14800	1100	$2.0\cdot10^{7}$	$4.3\cdot10^{5}$

face is estimated from these average counts taking into account the detector efficiency, the absorption of the PMMA, and the area of the pixel.

The difference in counts at the two energies is due to the smaller number of photons delivered by the tube at the energy of the second Bragg peak,[24] which is only partially compensated by the smaller absorption of the phantom and the larger efficiency of the silicon detector in edge configuration. The Alvarez–Macovski algorithm requires the acquisition of two images with similar statistics, and for such a phantom thickness (2 cm of PMMA) this condition is best matched for the 16–32 keV energies. Therefore, we expect the best results at 16–32 keV energies, while higher energy pairs would be better suited for larger thicknesses. In general, the optimal photon energies could be set as a function of the thickness of the investigated sample.[24]

The raw images shown in Figs. 6(a) and 6(b) should be corrected before applying the contrast cancellation algorithm. This has been done by means of a fully automatic correction procedure.

Two independent procedures have been developed using IGOR PRO 4.05A and MATLAB following the same scheme, but with slightly different technical implementations. The results obtained with the two methods are in excellent agreement. These procedures correct first for pixels where an error in the pseudo-random counters occurred, leading to a huge number of counts. These pixels appear as white pixels randomly distributed all over the image in Figs. 6(a) and 6(b) and present a much larger number of counts than the other pixels, so that they can be easily individuated by simple threshold filter and corrected with the interpolation of the counts of the two adjacent strips. Then a correction for the dead channels on the

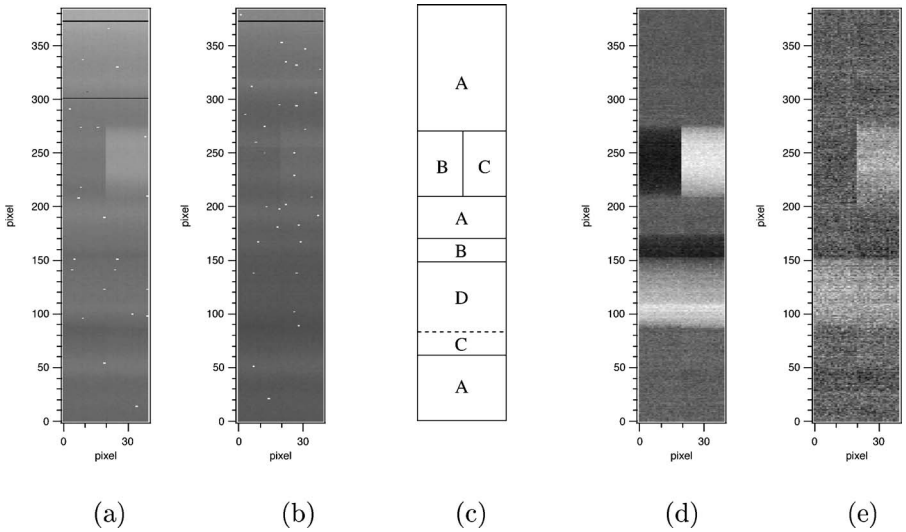

FIG. 6. (a) and (b) show the resulting images of the phantom, obtained with RX64DTH ASICs for $E_\ell = 16$ keV and $E_h = 32$ keV, respectively, before being corrected; (d) and (e) show the same images after being corrected. A scheme (c) of the resolved regions is also shown: (A) PMMA; (B) water; (C) polyethylene; (D) overlap of polyethylene and water.

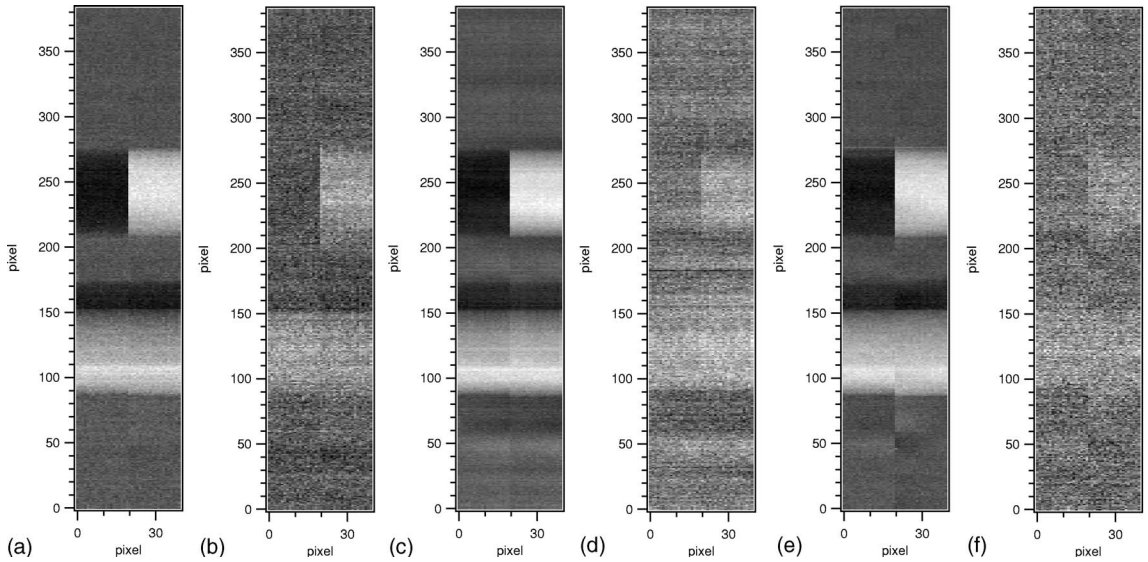

FIG. 7. Resulting experimental images with the RX64DTH ASICs for $E_\ell = 16$ keV (a) and $E_h = 32$ keV (b); $E_\ell = 18$ keV (c) and $E_h = 36$ keV (e) and $E_\ell = 20$ keV (d) and $E_h = 40$ keV (f).

counting ASICs [appearing as black horizontal lines in Figs. 6(a) and 6(b)] is applied. This correction is based on a "static" list of dead channels extracted from the ASIC test measurements. The dead pixels in the image are interpolated from the counts of the two contiguous strips.

A further correction is aimed at adjusting the statistical differences among different profiles, appearing in Figs. 6(a) and 6(b) as darker (lighter) vertical lines. These are due to fluctuations in x-ray intensity and sometimes also to bad synchronization between x-ray exposure and detector readout. This correction is extracted from the average counts of each profile in the uniform PMMA region of the phantom.

The high energy image counts thus corrected are subtracted from the low threshold image, thus obtaining the counts due only to the low energy photons. Finally, a correction is applied to account for the spatial distribution of the x-ray beam intensity and other artifacts related to the detecting system and the experimental setup which cause a nonuniform background. This correction is based on "white-field" profiles (one for each energy). These profiles have been collected for the RX64 based detector exposing the detector directly to the x-ray beam, while for the RX64DTH based detector the direct beam was attenuated by a uniform 2 cm PMMA absorber. Each phantom profile is divided by the corresponding white-field profile normalized to its average value.

Figures 6(d) and 6(e) show the images 6(a) and 6(b) after being corrected according to the procedure described above. As expected, water details are visible at low energy (16 keV) and not at high energy (32 keV). Figure 7 shows the experimental images for each energy pair, again for the detector equipped with the RX64DTH ASICs.

V. COMPUTER SIMULATIONS

A simulation of our experiment has been carried out with the MCNP-4C transport code[21] which is designed for transporting neutrons, photons, and electrons. The phantom and the detector have been simulated with their exact dimensions, including the 765-μm-thick inactive region of the detector in edge-on configuration.[27] A monochromatic parallel beam has been simulated in normal incidence on the phantom's front side. The energy dispersion of the quasi-monochromatic beam is neglected in these simulations. We expect that the absence of the energy dispersion contributes to making the quality of the simulated images better than that of the measured ones. The simulated beam is 4 cm long and 300 μm wide, so it covers a fraction of the phantom volume corresponding to the detector cross section.

In the simulation each incident photon is tracked until (a) it is totally absorbed within the phantom volume, (b) it is totally absorbed within the detector volume, or (c) it escapes from both of them. Also the electrons generated by the interaction of the incident photons with either the phantom or the detector are transported. The simulation of the interactions is based on the ENDF/B-VI data library. For each photon entering into the detector volume, every energy deposition event is recorded in a cumulative bin for each individual strip. Finally, counts-per-strip profiles just like the ones obtained on the experiment are created.

Due to the symmetry of the phantom, two profiles (one for each of the two halves of the phantom) are generated at each energy. The total number of simulated photons in each profile is of the order of 10^8 for an average simulation time of 9 h in a PC P-4, 1.5 GHz, resulting in $\sim 10^5$ photons on a transverse area of 300×100 μm^2 (equal to the pixel size). A 2D image of the simulated phantom (384×40 pixel matrix as the experimental images) is obtained by using 20 times each simulated profile adding an amount of Gaussian noise adjusted for each energy so as to reproduce the Poissonian fluctuations of the experimental images ($\sigma_{\text{Gauss}} = \sqrt{N_{\text{counts}}}$).

The resulting simulated images are shown in Fig. 8 for the three energy pairs used in the experimental measurements.

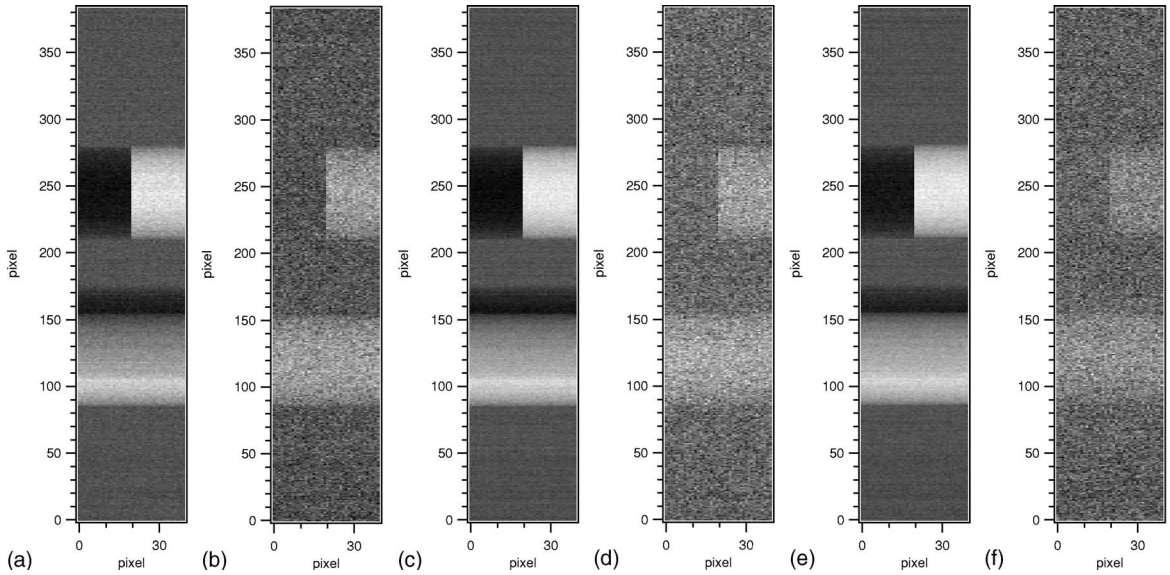

FIG. 8. Resulting simulated images for E_ℓ=16 keV (a) and E_h=32 keV (b); E_ℓ=18 keV (c) and E_h=36 keV (d) and E_ℓ=20 keV (e) and E_h=40 keV (f).

The simulated profiles in the left and right part of the phantom at the 16–32 keV energy setting are compared in Fig. 9 to the average profiles measured with the RX64DTH ASICs at the corresponding energies. The good agreement obtained between experiment and simulation confirms the quality of the geometry and material description in the simulation code.

The small systematic differences between the measured and simulated profiles can be understood as due to the x-ray energy spread of the experimental beam, which is neglected in the MCNP simulations, and also to a possible misalignment of the detector with respect to the center of the x-ray beam, resulting in a difference between the nominal and the real energy of the incident photons.

VI. IMAGE ANALYSIS AND SNR CALCULATION

In order to obtain the contrast cancellation angle and the projected images for each energy pair, the Alvarez–Macovski algorithm is used. As explained in Sec. II, PMMA and PE are chosen as basis materials. To apply the dual energy algorithm, a pixel-by-pixel knowledge of the logarithmic transmission $M=\ln(I_0/I)$ is required. The intensity I_0 of the incident beam at each energy has been calculated from the number of counts I_1 in a region of the phantom where only Plexiglas is present. I_0 is then extracted using the theoretical attenuation coefficient of Plexiglas at the corresponding energy. [We chose to evaluate I_0 from a region of the image where the phantom absorption is known and not simply from the white-field profiles in order to apply exactly the same procedure to both the experimental data and to the simulations (for which the white field does not exist). Furthermore, the experimental white-field data with the RX64DTH based detector were taken with a uniform 2 cm PMMA absorber upstream from the detector and not exposing the detector to the direct beam].

Hybrid images $\boldsymbol{C}$ are calculated pixel-by-pixel with the projection formula

$$\boldsymbol{C} = A_1 \cos\phi + A_2 \sin\phi, \tag{7}$$

where A_1 and A_2 are given by Eq. (4). The projection angle ϕ is varied from 20 to 70° in steps of 0.5° in order to search for the contrast cancellation angle value, where the contrast between two of the phantom materials vanishes in the hybrid image, thus enhancing the detectability of the third one.

In order to select the proper contrast cancellation angles, the signal-to-noise ratio (SNR) values for each material pair are calculated on the hybrid images as a function of the projection angle. The SNR is defined as the ratio between the signal contrast C_s and the noise contrast C_n. We assumed that the signal is represented by the relative difference of mean gray level calculated in two regions of the image containing the appropriate material pair. For example, the signal of water with respect to Plexiglas is given by

$$C_s^{\text{water/plexi}} = \frac{m_w - m_p}{m_p}, \tag{8}$$

where m_w and m_p are the average of the gray levels measured on homogeneous water and Plexiglas areas, respectively. The contrast of the relative noise has been evaluated on the area A of PMMA background in the top part of the images (38 $\times$90 pixels). This has been done dividing the area A in subimages of 5×5 pixels, corresponding to a sampling area for noise of 0.5×1.5 mm^2. For each subimage an average gray level m_i is calculated and then the average m and the standard deviation $\sigma(m)$ of the m_i values are used to define the noise contrast as

$$C_n = \frac{\sigma(m)}{m}. \tag{9}$$

The 5×5 pixel sampling area is chosen as a compromise between having high number of photons inside the sampling area (which would call for a large area) and the need of making a reasonable number of samplings (the larger the

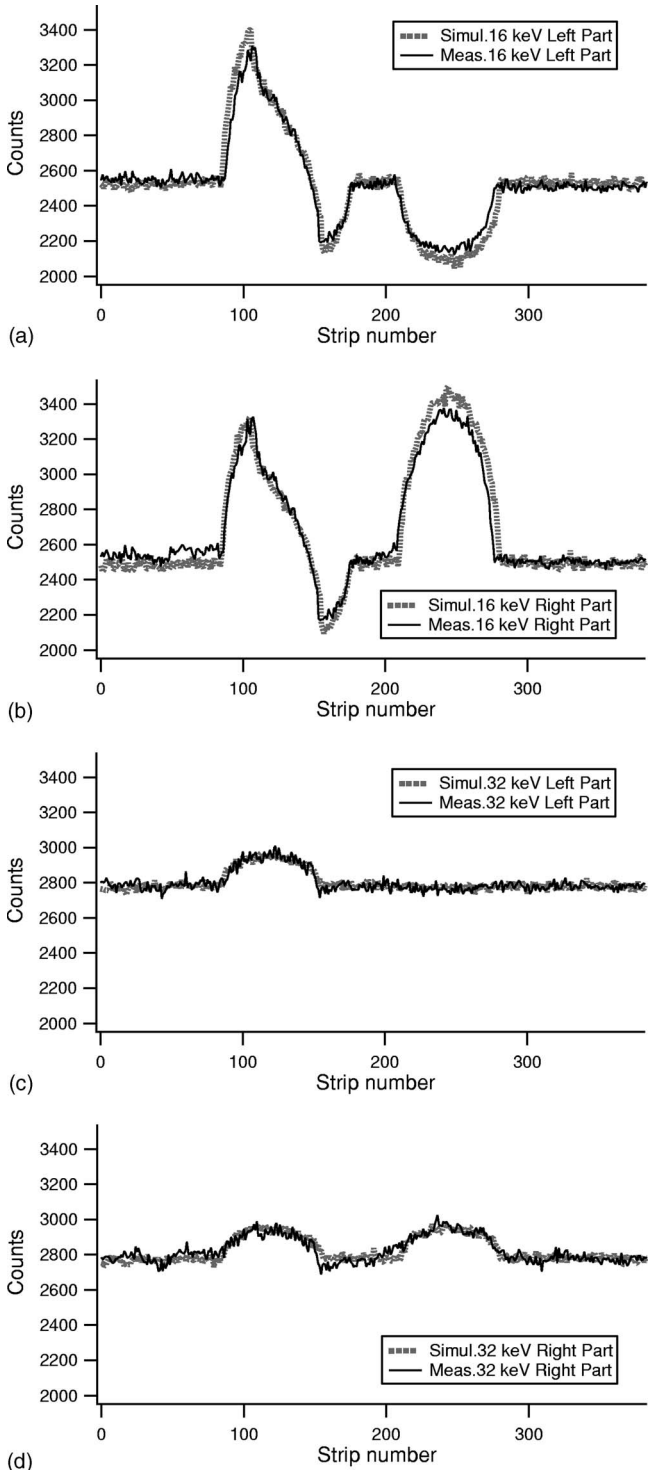

FIG. 9. Superposition of the average measured profiles with RX64DTH ASICs and the simulated ones at 16 keV (upper plots) and 32 keV (lower plots) for the left and right part of the phantom. The MCNP profiles are rescaled to the experimental ones using the average counts on all the strips.

sampling area, the smaller the number of samplings in the total area A). Furthermore, the geometrical size of the 5×5 pixel sampling area (0.5×1.5 mm^2) is comparable with the size of the interesting details in mammography.

By plotting SNR vs ϕ for a given energy setting, three curves corresponding to the three material pairs are obtained. Three angles ϕ which minimize the contrast between polyethylene and Plexiglas, between polyethylene and water and between Plexiglas and water, respectively, are thus found. These three angles represent the contrast cancellation angle for each pair of materials.

The evaluation of the SNR also allows to obtain quantitative information about the visibility of the details of a given material when the other two are forced to vanish. According to the Rose model,[31] a detail of an image with uniform background can be detected by the eye when its SNR exceeds a minimum value $\mathrm{SNR}_{\min}$. A typical value for the detectability threshold for human observers is found to be $\mathrm{SNR}_{\min}=5$. In the limit of low contrast (i.e., small differences between signal and background), the SNR is proportional to $\sqrt{N}\cdot C_s\cdot d$ where N is the number of photons generating the image, C_s is the signal contrast and d is the diameter of the detail of interest.[32] The smaller the detail of interest, the larger the signal contrast (which is constrained by the number of photons, i.e., by the dose delivered to the patient) needed to reach the detectability threshold $\mathrm{SNR}_{\min}$.

It has to be stressed that the projection at the angle for clutter removal does not, in general, maximize the contrast or the SNR, so that the maximum detectability may be achieved at an intermediate projection for which the drawbacks of some background clutter are compensated by a larger SNR.[10]

VII. RESULTS AND DISCUSSION

Figure 10 shows the SNR vs the projection angle ϕ plots for the measured (a) and simulated (b) data at $E_\ell=16$ keV and $E_h=32$ keV. It can be seen that the SNR curves as a function of the projection angle are compatible between experimental and simulated images. The SNR values of the experimental images are lower than the simulated ones, reflecting the presence of experimental features (such as finite white-field statistics, energy dispersion of the beam) which are not included in the MCNP simulations. [The white-field fluctuations are added to the image noise when correcting for the spatial distribution of x-ray beam intensity. In our case, the counts in the white-field profiles are 8000–20 000 (depending on the beam energy) giving rise to $\approx1\%$ Poissonian fluctuations]. In general, the Monte Carlo has proved to be able to reproduce the main features of our imaging system and this suggests the possibility of using MCNP simulations to evaluate the performance of the dual-energy projection algorithm in more realistic cases, such as phantoms simulating typical sizes and shapes of pathological formations.

The maximum of the curves which is visible in Fig. 10 at a projection angle $\phi=28.5°$ for the measured data ($\phi=29°$ for the simulations) is due to the fact that at this ϕ value the noise in the projected images has a minimum.[22] Hence, the projection at this angle, reported in Fig. 11, provides the best visibility of the details of all the three materials. This hybrid image can be useful for the study of phantom details because it provides complementary information with respect to the ones obtained by projecting at the contrast cancellation angles.

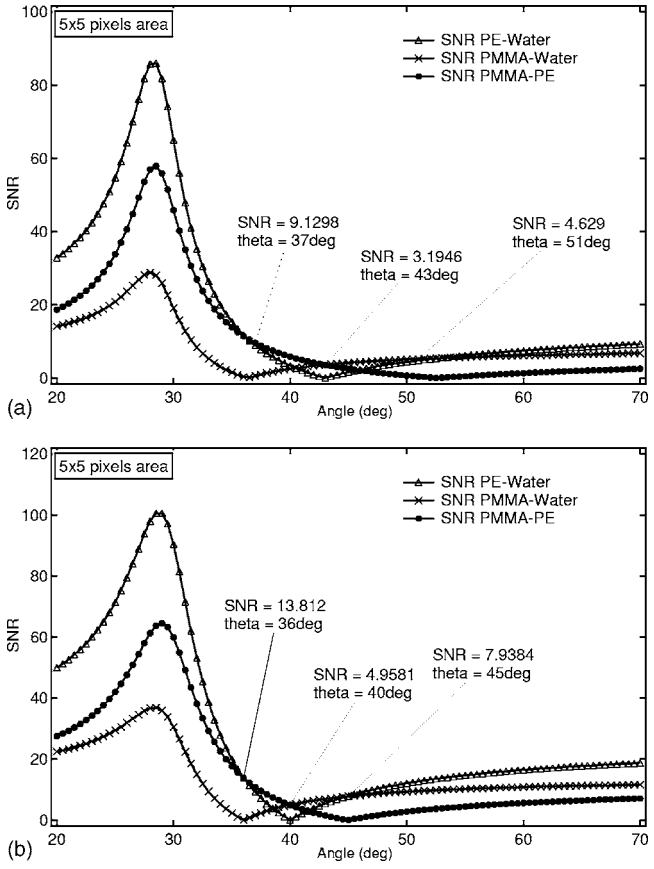

FIG. 10. SNR vs. ϕ plots for the measured (a) and simulated (b) data at E_ℓ=16 keV and E_h=32 keV.

The contrast cancellation angle for each material pair corresponds to the minimum of the corresponding curve in Fig. 10. Table IV shows the theoretical contrast cancellation angles compared to the ones obtained from the MCNP simulations and from the experimental data for the RX64 and RX64DTH based detectors. It can be seen that there is a good agreement (within 1.5°) between theoretical and simulated values of the contrast cancellation angle ϕ for each material pair at all energies. This result confirms the possibility of using the Alvarez–Macovski algorithm to enhance the visibility in mammographic images of a single material out of three. Also, when comparing the experimental values of the contrast cancellation angles and the theory, it can be seen that a good agreement is found at all energies. We verified that when moving the areas for contrast calculation inside the PMMA, PE and water regions of the phantom, the contrast cancellation angle values vary by ±1.5° with respect to the ones reported in Table IV.

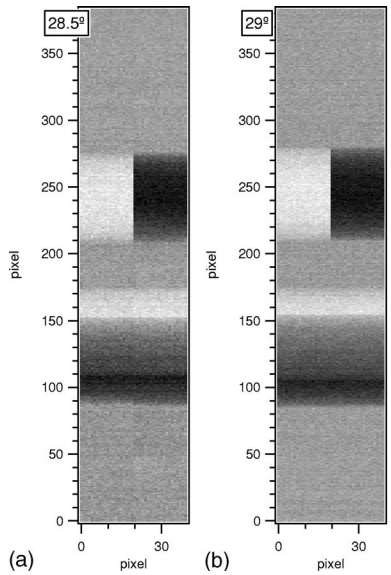

FIG. 11. Hybrid images at the projection angle which minimize the noise for (a) measured with the RX64DTH ASIC and (b) simulated data at E_ℓ =16 keV and E_h=32 keV.

TABLE IV. Comparison between theoretical, simulated, and experimental contrast cancellation angles ϕ values.

Energy (keV)	Material pair	Theoretical	MC	Experimental	
				RX64	RX64DTH
	PMMA-Water	36.5°	36.0°	35.0°	37.0°
16–32	PE-Water	40.5°	40.0°	40.0°	43.0°
	PE-PMMA	45.0°	45.0°	46.0°	51.0°
	PMMA-Water	36.5°	35.5°	38.0°	35.5°
18–36	PE-Water	40.5°	40.5°	43.5°	40.0°
	PE-PMMA	45.0°	48.0°	51.5°	46.0°
	PMMA-Water	36.5°	35.5°	38.5°	37.0°
20–40	PE-Water	40.5°	39.5°	42.5°	41.0°
	PE-PMMA	45.0°	44.0°	45.0°	46.0°

Table V summarizes the SNR values extracted from the images acquired with the RX64 and the RX64DTH based detectors at the measured cancellation angles reported in Table IV. The sampling area for noise is 5×5 pixels. A variation of about ±20% of the SNR values is observed when moving the areas for contrast calculations inside the PMMA, PE, and water regions of the phantom. The better performance of the RX64DTH ASIC (which allows to acquire the images at the two energies within the same exposure) makes it possible to obtain comparable values of SNR with about half of the incident photons.

TABLE V. Values of SNR at the measured contrast cancellation angles. The sampling area for noise is 5×5 pixels.

Energy (keV)	Canceled materials	Contrast material	SNR	
			RX64	RX64DTH
	PMMA-Water	PE	8.11	9.13
16–32	PE-Water	PMMA	2.53	3.19
	PE-PMMA	Water	3.96	4.63
	PMMA-Water	PE	7.43	6.98
18–36	PE-Water	PMMA	2.70	2.40
	PE-PMMA	Water	3.85	4.07
	PMMA-Water	PE	2.55	5.24
20–40	PE-Water	PMMA	0.67	1.81
	PE-PMMA	Water	0.89	2.93

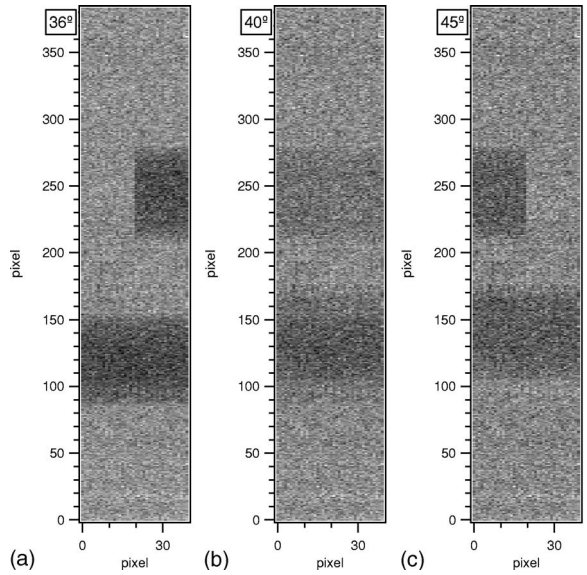

FIG. 12. Projected images corresponding to the contrast cancellation angle between PMMA and water (a) water and PE (b) PMMA and PE (c) for simulated images at $E_\ell = 16$ keV and $E_h = 32$ keV.

The experimental SNR values are limited mainly by the poor statistics of high energy images (32, 36, and 40 keV). For this reason, the best performance is obtained, as expected, with the 16–32 keV energy pair, which has the largest number of photons in the high energy image. At this energy setting, the SNR of water details ($4.63 \pm 20\%$) is practically coincident with the detectability threshold while the SNR of polyethylene details is well above it.

Figure 12 shows the hybrid images obtained projecting the images simulated at $E_\ell = 16$ keV and $E_h = 32$ keV using the contrast cancellation angles reported in Table IV. The left panel (a) shows the image at the cancellation angle between PMMA and water: the contrast between PMMA and water has been made to vanish and only the PE can be seen. In the middle panel (b), water and PE are forced to the same gray level and the PMMA contrasts with them. In the right panel (c), the water is isolated. The hybrid images obtained projecting the images collected with the RX64DTH ASICs at the 16–32 keV energy setting are shown in Fig. 13.

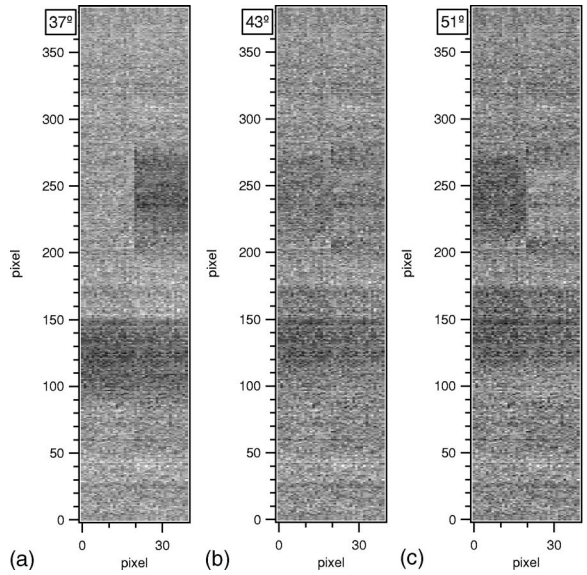

FIG. 13. Projected images corresponding to the contrast cancellation angle between PMMA and water (a) water and PE (b) PMMA and PE (c) for measured images at $E_\ell = 16$ keV and $E_h = 32$ keV.

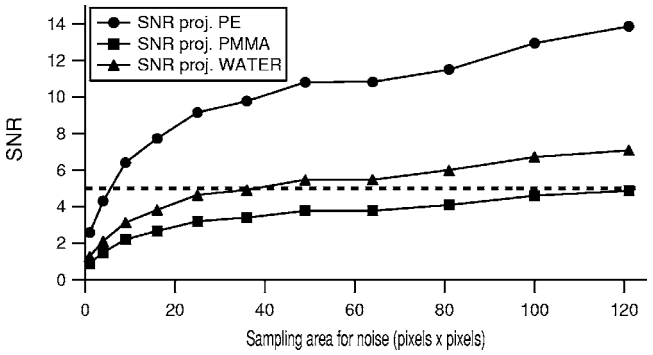

FIG. 14. SNR vs. size of the sampling area for noise at the 3 contrast cancellation angles for experimental images at 16–32 keV energy pair. The dotted line represents the SNR=5 detectability threshold according to Rose model.

A study of the SNR value as a function of the size of the sampling area for noise has been performed on the experimental images collected at the 16–32 keV energy pair. The results are shown in Fig. 14 which shows the value of SNR measured at the three contrast cancellation angles when varying the sampling area for noise from 1 to 121 (11×11) pixels. The SNR increases when the sampling area of noise increases following the expected $\sqrt{N_{\text{pixels}}}$ trend and reflecting the better visibility of a larger detail with respect to a small one having the same contrast.[31] The SNR=5 detectability threshold is also shown in the plot (dotted line) and it can be used to estimate the minimal size of a detail which can be detected on the hybrid images. In the case of the projection at the contrast cancellation angle between PE and PMMA, only water details (which mimic cancerous tissue) are visible in the hybrid image. The minimum size of the water area which is visible in the hybrid image (SNR above 5) is of the order of 30 pixels.

VIII. CONCLUSIONS

Dual energy mammographic imaging experimental tests have been performed using a compact dichromatic source based on a conventional x-ray tube and a mosaic crystal. The selected pairs of x-ray energies were 16–32, 18–36, and 20–40 keV, so as to have the low energy photons in the optimum range for mammography application. The two beams are superimposed in space and the high energy is twice the value of the low energy due to the Bragg-diffraction technique used to obtain the dual-energy beam. Two detector prototypes based on an array of 384 silicon microstrips coupled to the RX64 and RX64DTH ASICs for single photon counting have been used for detecting the x rays. In particular, the RX64DTH ASIC, providing an energy resolution of ~1 keV and the capability of counting low

energy x rays within two selectable energy windows, is well adapted to dual-energy imaging techniques. The double threshold discriminator implemented in the RX64DTH ASIC allows the acquisition of the two x-ray energies within the same exposure, thus enhancing the quality of the images with respect to the single threshold RX64 ASIC.

The Alvarez–Macovski algorithm has been successfully tested on images obtained from a mammographic phantom consisting of three materials (PMMA, PE, and water, resembling glandular, fat, and cancerous tissues, respectively). The results obtained both from MCNP simulated and experimental images show contrast cancellation between two materials, thereby enhancing the visibility of small features in the third one. The values of SNR obtained on a 5×5 pixel area (corresponding to a sampling area for noise of 0.5×1.5 mm^2) with a statistics $\leqslant$10 000 total photons/pixel indicate that the contrast cancellation technique is a powerful tool which can be very well suited for medical applications, like, e.g., dual energy mammography, where it could improve the clinical ability of detecting breast cancer in the cases in which the conventional examination leads to an uncertain diagnosis.

The agreement obtained between MCNP results and the experimental data suggests the possibility of using Monte Carlo simulations to investigate the performance of our imaging system in more realistic cases. For example, the dual-energy projection algorithm could be applied to simulated images of more realistic phantoms (resembling typical shapes and sizes of cancerous formations) in order to evaluate the effective advantages of dual-energy techniques.

The results presented in this paper demonstrate the feasibility of dual-energy imaging with the quasi-monochromatic x-ray source and a silicon microstrip detector with single photon counting capability. Further efforts should be made to optimize the x-ray source and the detector in order to guarantee the clinical viability of this technology. In particular, it would be important to increase the counting statistics of experimental measurements, especially at the higher energy, since the lack of statistic at the higher energy appears to be the main limit of the measured SNR values. Several important issues for clinical practice (like, for example, tube heating limitation, parallax errors due to beam divergence, and dose studies) are still under investigation.

ACKNOWLEDGMENTS

This work was supported in part by the Polish State Committee for Scientific Research under Grant No. 3T11B01427, the TRIL programme from ICTP Trieste and the European Commission ALFA programme Contract No. AML/B7-311/97/0666/II-0042FA.

[a]Author to whom correspondence should be addressed; electronic mail: prino@to.infn.it

[1]G. Hermann *et al.*, "Occult malignant breast lesion in 114 patients: relationship to age and the presence of microcalcification," Radiology **169**, 321–324 (1988).
[2]A. Fandos-Morera *et al.*, "1988 Breast tumor: composition of microcalcifications," Radiology **169**, 325–327 (1988).
[3]R. H. Harrison, "Digital radiography—a review of a detector design," Nucl. Instrum. Methods Phys. Res. A **310**, 23–34 (1991).
[4]F. Arfelli *et al.*, "A linear array silicon pixel detector: images of a mammographic test object and evaluation of delivered doses," Phys. Med. Biol. **42**, 1565–1573 (1997).
[5]D. G. Darambara *et al.*, "Preliminary evaluation of a prototype stereoscopic *a*-Si:H-based x-ray imaging system for full-field digital mammography," Nucl. Instrum. Methods Phys. Res. A **471**, 285–289 (2001).
[6]T. Francke *et al.*, "Dose reduction in medical x-ray imaging using noise free photon counting," Nucl. Instrum. Methods Phys. Res. A **471**, 85–87 (2001).
[7]R. D. Speller *et al.*, "Digital x-ray imaging using silicon microstrip detectors: a design study," Nucl. Instrum. Methods Phys. Res. A **457**, 653–664 (2001).
[8]R. E. Alvarez and A. Macovski, "Energy-selective reconstruction in x-ray computerized tomography," Phys. Med. Biol. **21**, 733–744 (1976).
[9]L. A. Lehmann *et al.*, "Generalized image combinations in dual KVP digital radiography," Med. Phys. **8**, 659–667 (1981).
[10]P. C. Johns and M. J. Yaffe, "Theoretical optimization of dual energy x-ray imaging with application to mammography," Med. Phys. **12**, 289–296 (1985).
[11]P. C. Johns *et al.*, "Dual energy mammography: initial experimental results," Med. Phys. **12**, 297–304 (1985).
[12]J. M. Boone, G. S. Shaber, and M. Tcotzky, "Dual energy mammography: a detector analysis," Med. Phys. **17**, 665–675 (1990).
[13]M. Gambaccini *et al.*, "Narrow energy band x-rays via mosaic crystal for mammography application," Nucl. Instrum. Methods Phys. Res. A **365**, 248–254 (1995).
[14]W. Dabrowski *et al.*, "A read out system for position sensitive measurements of x-ray using silicon strip detectors," Nucl. Instrum. Methods Phys. Res. A **442**, 346–354 (2000).
[15]P. Grybos and W. Dabrowski, "Development of fully integrated readout system for high count rate position sensitive measurements of x-rays using silicon strip detectors," IEEE Trans. Nucl. Sci. **48**, 466–472 (2001).
[16]P. Grybos *et al.*, "Multichannel mixed-mode IC for digital readout of silicon strip detectors," Microelectron. Reliab. **42**, 427 (2002).
[17]D. Bollini *et al.*, "Energy resolution of a silicon detector with the RX64 ASIC designed for x-ray imaging," Nucl. Instrum. Methods Phys. Res. A **515**, 458–466 (2003).
[18]P. Grybos *et al.*, "RX64DTH-A fully integrated 64-channel ASIC for a digital x-ray imaging system with energy window selection," IEEE Trans. Nucl. Sci. **52** (4), 839–846 (2005).
[19]G. Baldazzi *et al.*, "Results about imaging with silicon strips for Angiography and Mammography," AIP Conf. Proc. **682**, 14–23 (2003).
[20]A. E. Cabal Rodriguez *et al.*, "x-ray imaging with a single photon counting system," *Proc. EXRS 2004 Eur. Conf. on x-Ray Spectrometry*, Alghero, Italy, 2004.
[21]"MCNP 4C-Monte Carlo N-Particle Transport Code System," RSICC Computer Code Collection, Oak Ridge National Laboratory (2001).
[22]S. Fabbri *et al.*, "Signal-to-noise ratio evaluation in dual-energy radiography with synchrotron radiation," Phys. Med. Biol. **47**, 4093–4105 (2002).
[23]M. Marziani *et al.*, "Dual-energy tissue cancellation in mammography with quasi-monochromatic x-rays," Phys. Med. Biol. **47**, 305–313 (2002).
[24]A. Tuffanelli *et al.*, "Evaluation of a dichromatic x-ray source for dual-energy imaging in mammography," Nucl. Instrum. Methods Phys. Res. A **489**, 509–518 (2002).
[25]M. Gambaccini *et al.*, "Spatial resolution measurements in quasimonochromatic x rays with mosaic crystals for mammography application," Med. Phys. **28**, 412–418 (2001).
[26]P. C. Johns and M. J. Yaffe, "x-ray characterization of normal and neoplastic breast tissues," Phys. Med. Biol. **32**, 675–695 (1987).
[27]G. Baldazzi *et al.*, "A silicon strip detector coupled to the RX64 ASIC for x-ray diagnostic imaging," Nucl. Instrum. Methods Phys. Res. A **514**, 206–214 (2003).
[28]G. Baldazzi *et al.*, "Dual energy imaging in mammography: Cross-talk study in a Si array detector," Nucl. Instrum. Methods Phys. Res. B **213**, 603–606 (2004).
[29]"IGORPRO 4.05A," WaveMetrics Inc., Lake Oswego, Oregon.
[30]"MATLAB computing language" MathWorks, Natick, MA, USA.
[31]A. Rose, *Vision: Human and Electronic* (Plenum, New York, 1973).
[32]S. Smith *et al.*, "Low contrast detectability and contrast/detail analysis in medical ultrasound," IEEE Trans. Sonics Ultrason. **30**, 164–173 (1983).